Complex dynamical interplay between solid particles and flow in driven granular suspensions

Sadato Yamanaka, Akira Furukawa, and Hajime Tanaka*
Department of Fundamental Engineering, Institute of Industrial Science, University of Tokyo, 4-6-1 Komaba, Meguro-ku, Tokyo 153-8505, Japan

(Received 27 July 2018; published 23 July 2019)

Granular materials immersed in a fluid are ubiquitous in daily life, industry, and nature. They include food processing, pastes, cosmetics, paints, concretes, cements, muds, wet sands, snows, landslides, and lava flow. They are known to exhibit a rich variety of complex rheological behavior, but the role of a fluid component in such behavior has remained poorly understood due to the nonlocal and many-body nature of hydrodynamic interactions between solid particles mediated by the fluid. We address this fundamental problem by comparing the microrheological response of athermal granular suspensions with and without hydrodynamic interactions to an externally driven probe particle by numerical simulations. We find that the presence of the fluid drastically increases the drag coefficient of the probe particle by more than one order of magnitude near the jamming transition. We reveal that this is a consequence of the nontrivial long-range nature of hydrodynamic interactions, which originates from unlimited cumulative transmission of near-field hydrodynamic interactions due to the incompressibility of both fluid and solid particles. Force chain formation of solid particles is dynamically coupled with hydrodynamic flow, leading to strong spatiotemporal fluctuations of flow pattern and nonlinear rheological response. Our study reveals essential roles of hydrodynamic interactions in complex rheological behavior of dense granular suspensions under an external drive.

DOI: 10.1103/PhysRevE.100.012907

I. INTRODUCTION

Dense athermal suspensions behave as elastic solids above the so-called jamming point, whereas they behave as viscous fluids under strong-enough loading: Such behavior can be commonly seen in immersed granular materials, pastes, emulsions, and foams [1–21]. The solid-to-liquid transition induced by external loading, known as yielding, is important not only in processing of materials and foods but also in geological phenomena such as liquefaction and land sliding and biological phenomena such as the active motion of micro creatures in mud and wet sand. When approaching the jamming transition, the viscosity of suspensions steeply diverges. The jamming takes place as a consequence of self-organization of force network with isostaticity. Even before the jamming transition, temporal force chains start to play a crucial role in the viscoelastic response of dense suspensions [1,22,23], including yielding [24,25] and abrupt shear thickening [26–30]. The presence of force chains leads to complex rheological behaviors essentially different from ordinary simple fluids.

In suspensions of frictionless particles, force chains are formed by solid particles with direct mechanical interactions. On the other hand, the other component of a suspension, a liquid, should also play a crucial role in the rheological response [9,15] since the dissipation should take place exclusively in the fluid for a system of frictionless particles. However, the role of hydrodynamic interactions mediated by the fluid, has remained elusive, due to theoretical and technical difficulties in modeling many-body hydrodynamic effects properly and/or to an expectation for screening of long-range hydrodynamic interactions by dense solid particles [31,32].

For example, the exponential screening is rather well established for polymer solutions [33]. This may also be the case if solid particles are fixed in space, since flow is randomized by them. However, this expectation is highly questionable in general, although the situation has been a bit controversial [32,34,35]. It is natural to expect that nonlocal hydrodynamic effects should play a crucial role in the rheological response of dense suspensions through a strong kinetic constraint on particle rearrangements. So far, however, this problem has not attracted much attention and the rheological behavior of athermal suspensions has often been discussed on the basis of mechanical interactions between solid particles, or force chains, neglecting the nonlocal hydrodynamic nature of energy dissipation.

In this article, we address this fundamental problem by using numerical simulations. We stress that there is a crucial difference between polymers and colloids: For the former we can assume the point-force assumption for each monomer and represent the velocity field created by it by the Oseen tensor [33], whereas for the latter this is not the case because a colloid particle has a finite volume and is incompressible. Below we will show that this leads to the following nontrivial hydrodynamic effects in dense suspensions. The incompressibility has hierarchical roles in dense suspension: near-field hydrodynamic interactions via the incompressibility of the solvent and their transmission through that of both the solvent and solid host particles. First, the incompressibility of a fluid induces squeezing effects when particles approach each other, tending to prevent direct contacts [36–40]: near-field

*tanaka@iis.u-tokyo.ac.jp

hydrodynamic interactions. More importantly, the incompressibility means the absence of an endpoint of flow line. This suggests that the particle configuration in a suspension is to be self-organized by flow, resulting in long-range spatiotemporal correlations. We note that the nature of the long-range correlations is essentially different from that of unscreened bare hydrodynamic interactions. Bare hydrodynamic interactions are indeed disturbed by the presence of particles, but this is not the end of story. By a completely different mechanism, near-field hydrodynamic interactions propagate in a *cumulative* manner over an unlimited range through the incompressbility of the solvent and solid particles, resulting in the nontrivial long-range nature of the interactions.

II. MICRORHEOLOGICAL APPROACH

To elucidate the essential role of hydrodynamic interactions, we take an active microrheological approach to dense athermal suspensions. The microrheological approach is a very powerful means to elucidate the rheological response of both thermal and athermal systems. It has been established that there is a one-to-one correspondence between microrheological and macroscopic approaches in the linear response regime of thermal systems [41–43]. For an athermal system, there is a causal relation between an external perturbation and the response to it. It was also shown both theoretically [44–46] and experimentally [47,48] that nonlinear shear thinning behavior can also be accessed by microrheology. Thinning behavior is often accompanied by asymmetry in the particle configuration around the driven probe particle, but the exact origin still remains elusive. The importance of lubricational effects under a strong drag was also pointed out [45,46,49]. The importance of hydrodynamic interactions in microrheological behavior has been well recognized, and there are many interesting studies [10,18,21,44–46,50–54]. However, most of previous works were limited to semi-dilute suspensions or highly approximated the many-body nature of hydrodynamic interactions. Thus, it has remained unclear how hydrodynamics spatiotemporally organize host particles and how such dynamical organization behavior affects the rheological properties.

On the other hand, microrheological approaches to dry granular media [55–59] and the method of intruder impaction onto granular beds [60–62], have been established to investigate the local response of granular media to the probe motion via force chains. For dry systems, the probe particle experiences direct collisions with the surrounding particles on its motion. This results in repeated formation and collapse of force chains, and their mechanical stability controls dominantly the flow behaviors. In this study, we put a particular focus on the role of the hydrodynamic degree of freedom to answer the fundamental questions such as how hydrodynamic interactions affect the stability of force chains and how fluid flow and force chains dynamically interact.

We study the rheological response of a suspension to the motion of a probe particle driven by a constant external force [63] for systems with and without hydrodynamic interactions by numerical simulations. To this end, we perform numerical simulations in two dimensions to see structural organization clearly. In our microrheological approach, there are two key parameters: the volume fraction of solid particles, Φ, and the drag force, F, that is always applied to the center of mass of the probe particle along x direction. We employ two numerical simulation methods: (1) the fluid particle dynamics (FPD) method [36], which fully incorporates many-body hydrodynamic interactions, and (2) the relaxation dynamics (RD) method, in which hydrodynamic interactions are completely neglected and only the dissipation due to the particle-solvent relative motion is taken into account as a constant local friction coefficient, whose magnitude is set to be equal to the Stokes friction of a single particle immersed in the same solvent. The details of our system and FPD and RD methods are explained in the next section.

III. METHODS

A. Setup of the system

The setup of the model system studied is as follows. We use a two-dimensional (2D) model suspension of non-Brownian particles, which is a binary mixture of two types of circular disks, A and B. To avoid crystal ordering, the ratio of radius between the two species is set as $a_A/a_B = 1.4$, and the number of particles is approximately the same: $N_A \approx N_B$. In a system containing $N = N_A + N_B$ particles in total, one of the larger particles A is selected as a *probe* particle and dragged by a constant external force $\boldsymbol{F}$ along x axis. Hereafter, the index of the probe particle is set as $i = 1$, and we refer to the other $N - 1$ particles as *host* particles. The particles interact via a soft-core repulsive potential defined as

$$U(\boldsymbol{R}_{ij}) = \epsilon\left(\frac{\sigma_{ij}}{R_{ij}}\right)^{36}, \tag{1}$$

with $\sigma_{ij} = a_i + a_j$, $\boldsymbol{R}_{ij} = \boldsymbol{R}_i - \boldsymbol{R}_j$, and $R_{ij} = |\boldsymbol{R}_{ij}|$, where a_i is the particle radius and $\boldsymbol{R}_i$ the center of mass of particle i. Our focus is on athermal suspensions of frictionless particles, and thus there are neither thermal fluctuations nor contact friction between particles.

We perform simulations in two-dimensional square systems under periodic boundary conditions. To check the finite-size effects, the linear dimension L is varied as $L = 64$, 128, 256, and 512 for FPD and as $L = 64$, 128, 256, 512, and 1024 for RD. The volume fraction is defined as $\Phi = \pi(N_A a_A^2 + N_B a_B^2)/L^2$. All of the numerical simulations are started from random particle configurations, and the drag force is imposed at the start of each simulation.

B. Fluid particle dynamics

In order to take the hydrodynamic degrees of freedom into account, we use the FPD method [36–39], a hybrid numerical method where the Navier-Stokes equation for fluid dynamics and the equations of the motions of particles are numerically solved on-lattice and off-lattice, respectively. In this method, solid particles are approximated by undeformable highly viscous fluid particles, whose viscosity η_p is much larger than that of the solvent η_s. The viscosity field is defined as

$$\eta(\boldsymbol{r}) = \eta_s + \sum_{i=1}^{N}(\eta_p - \eta_s)\phi_i(\boldsymbol{r}). \tag{2}$$

The viscosity change across the interface of particle i is represented by a smooth hyperbolic tangent function:

$$\phi_i(\boldsymbol{r}) = \frac{1}{2}\left[\tanh\left(\frac{a_i - |\boldsymbol{r} - \boldsymbol{R}_i|}{\xi_i}\right) + 1\right], \tag{3}$$

where ξ_i is the thickness of the particle interface. The time evolution of the velocity field $\boldsymbol{v}(\boldsymbol{r})$ obeys the momentum conservation equation or the Navier-Stokes equation:

$$\rho\left(\frac{\partial}{\partial t} + \boldsymbol{v}\cdot\nabla\right)\boldsymbol{v} = \nabla\cdot\overleftrightarrow{\sigma} + \boldsymbol{f}_p + \boldsymbol{f}_d, \tag{4}$$

where the mass density ρ is uniform over the system. The stress tensor $\overleftrightarrow{\sigma}$ is defined, using the viscosity field (2), as

$$\overleftrightarrow{\sigma} = -p\overleftrightarrow{I} + \eta[\nabla\boldsymbol{v} + (\nabla\boldsymbol{v})^t], \tag{5}$$

where $\overleftrightarrow{I}$ represents a unit tensor. The pressure $p(\boldsymbol{r})$ is calculated so as to satisfy the incompressibility condition $\nabla\cdot\boldsymbol{v}(\boldsymbol{r}) = 0$. $\boldsymbol{f}_p(\boldsymbol{r})$ is the force density field due to the particle interaction and is given by

$$\boldsymbol{f}_p(\boldsymbol{r}) = \sum_{i=1}^{N}\frac{\boldsymbol{F}_i^p\phi_i(\boldsymbol{r})}{\Omega_i}, \tag{6}$$

where $\Omega_i = \int d\boldsymbol{r}\phi_i(\boldsymbol{r})$ is the area of particle i and $\boldsymbol{F}_i^p = -\sum_{j\neq i}\partial U(\boldsymbol{R}_{ij})/\partial\boldsymbol{R}_{ij}$ is the interparticle potential force acting on particle i. $\boldsymbol{f}_d(\boldsymbol{r})$ is an external constant drag force acting on the probe particle ($i = 1$, which we denote by the suffix p), which is given by

$$\boldsymbol{f}_d(\boldsymbol{r}) = \frac{F\phi_p(\boldsymbol{r})}{\Omega_p}\hat{\boldsymbol{e}}_x, \tag{7}$$

with $\hat{\boldsymbol{e}}_x$ the unit vector along the x axis. Furthermore, we introduce $\boldsymbol{f}_d' = -F/L^2\hat{\boldsymbol{e}}_x$, which is a superficial force on each lattice, to guarantee that the center of mass of the system is fixed, i.e., the momentum of the system is conserved. We note that this term is negligible for a very large system size. This term modifies Eq. (10) to add a term $-\frac{\Omega_i}{L^2}F\hat{\boldsymbol{e}}_x$ and Eq. (13) to add $-\frac{\Omega_p}{L^2}F\delta_{i1}\hat{\boldsymbol{e}}_x$. As shown in Eqs. (6) and (7), the central forces acting on particles are mapped onto the lattice points inside the particles and thus can be treated as the field variable.

The velocity of the center of mass of particle i is given by the average of the fluid velocity inside the particle as

$$\boldsymbol{V}_i(t) = \frac{1}{\Omega_i}\int d\boldsymbol{r}\phi_i(\boldsymbol{r})\boldsymbol{v}(\boldsymbol{r},t). \tag{8}$$

Then the particle is translated off the lattice by the following equation:

$$\frac{d\boldsymbol{R}_i}{dt} = \boldsymbol{V}_i(t), \tag{9}$$

and the viscosity field (2) is updated with the ϕ_i field obtained by new particle positions $\boldsymbol{R}_i$. We repeat this procedure successively to follow the dynamic evolution of the system.

In the FPD method, if the ratio η_p/η_s is sufficiently large and ξ_i/a_i small, then we can safely assume that the particles behave as solid ones. Since we treat a particle as a liquid particle, the FPD method effectively satisfies the solid-liquid nonslip boundary condition, which is the key to simplify our simulation with full many-body hydrodynamic interactions. We also stress that our method can satisfy the incompressible condition almost perfectly.

To physically justify our method, we derive an approximate equation of motion for particle i below. By multiplying both sides of Eq. (4) by $\phi_i(\boldsymbol{r})$ and spatially integrating over the system, one derives

$$M_i\frac{d\boldsymbol{V}_i}{dt} = \int d\boldsymbol{r}\phi_i\nabla\cdot\overleftrightarrow{\sigma} + \frac{\Omega_i'}{\Omega_i}\boldsymbol{F}_i^p + \frac{\Omega_p'}{\Omega_p}F\delta_{i1}\hat{\boldsymbol{e}}_x, \tag{10}$$

with particle mass $M_i = \rho\Omega_i$ and $\Omega_i' = \int d\boldsymbol{r}\phi_i^2(\boldsymbol{r})$. The first term in the right-hand side is the force exerted by the fluid including hydrodynamic interactions. The second term is the interparticle force, whose magnitude is corrected to take the finite thickness of particle surfaces into account. The Kronecker delta in the third term indicates that the external drag force is acting only on the probe particle.

The units of time τ and length ℓ are considered to satisfy a relationship

$$\tau = \frac{\rho\ell^2}{\eta_s}, \tag{11}$$

which sets both the density and viscosity of the fluid part to unity. This τ is a time required for the fluid momentum to diffuse over distance ℓ. The units of stress and force are $\overline{\sigma} = \rho(l/\tau)^2$ and $\overline{f} = \rho\ell/\tau^2$, respectively. In our simulations, the parameters are fixed as follows: $a_A = 8.96$, $a_B = 6.4$, $\rho = 1$, $\eta_p = 50$, $\eta_s = 1$, $\xi_i = 1$, and $\epsilon = 1$. The lattice size is $\Delta = \ell = 1$, and the time increment is $\Delta t = 0.004$ for $L \leqslant 256$ and 0.005 for $L = 512$.

Here we note that the size of a small B particle $a_B = 6.4$, which is composed of about 130 lattices, is large enough for our purposes. Moreover, the characteristic time of particle motion, $\tau_{\rm ch} = a_B/V_{\rm px}$, is much slower than the time required for momentum diffusion in a particle B, $\tau_{\rm diff} = a_B^2/(\eta_p/\rho)$. The ratio $\mathrm{Re} = \tau_{\rm diff}/\tau_{\rm ch} = \rho V_{\rm px}a_B/\eta_p \lesssim 0.01$ even at a very low Φ (=0.038), where the partcle moves very fast. Thus, we may safely assume that the velocity fields inside the particles are equilibrated in the timescale of their motions.

C. Relaxation dynamics

The RD method completely neglects interparticle hydrodynamic interactions. The contribution of a fluid on particle motion is only through a constant friction coefficient ζ_i. Instead of Eq. (10), the center of mass $\boldsymbol{R}_i$ and the velocity $\boldsymbol{V}_i$ of particle i obeys the following equations:

$$\frac{d\boldsymbol{R}_i}{dt} = \boldsymbol{V}_i, \tag{12}$$

$$M_i\frac{d\boldsymbol{V}_i}{dt} = -\zeta_i\boldsymbol{V}_i + \frac{\Omega_i'}{\Omega_i}\boldsymbol{F}_i^p + \frac{\Omega_p'}{\Omega_p}F\delta_{i1}\hat{\boldsymbol{e}}_x. \tag{13}$$

Here we note that in this case we do not need to introduce the superficial forces, which are considered in the FPD method. Moreover, the rotational degree of freedom is neglected. There is an exact match in the timescale of single-particle motion between the FPD and RD methods in a dilute limit.

The units of time τ and length ℓ are chosen to be the same as in the FPD method. We also employ the same parameters

TABLE I. The drag coefficient of a probe particle in the FPD method for different system size L and radius of probe particle a_p. No host particles are suspended. The magnitude of the drag force is $F = 0.5$.

L	a_p	$C_D^{(1)}$
64	8.96	18.38081
64	6.4	12.67436
128	8.96	9.340263
128	6.4	7.393265
256	8.96	6.509153
256	6.4	5.482283
512	8.96	5.288024
512	6.4	4.588942

a_A, a_B, ξ_i, and ϵ as those used in the FPD method. The time increment in the RD simulations is set as $\Delta t = 0.001$.

D. Drag coefficient of the driven probe particle

In two-dimensional systems, the Stokes drag law is known to be broken, and the drag coefficient is a function of not only the steady velocity but also the system size [64]. In our simulations, the friction coefficient ζ_i in RD is set to be equal to the drag coefficient that is calculated by FPD for a single-particle system, i.e., a system with no host particles. The values are summarized in Table I for various system sizes L and for probe radii a_p (see also Appendix B and Fig. 8).

We can see that the drag coefficients are larger when either the system size L is smaller or the particle radius a_p is larger, which qualitatively agree with a 2D hydrodynamic theory including finite-size effects [64].

In the present study, the rheological properties of a suspension are characterized by the drag coefficient of the probe particle. The average probe velocity is obtained by the time average of the probe velocity along the direction of the drag force in a steady state: $V_{px} = \langle V_{px}(t)\rangle_t$, where $\langle X\rangle_t$ represents the time average of a quantity X. Then the effective drag force acting on the probe particle is defined as $F_{\rm eff} = \Omega_p' F/\Omega_p$. Thus, the drag coefficient is obtained as

$$C_D = \frac{F_{\rm eff}}{V_{px}}. \tag{14}$$

This definition is common in both the FPD and RD method.

IV. IMPACT OF HYDRODYNAMICS ON THE PROBE PARTICLE MOTION IN DENSE SUSPENSIONS: TIME-AVERAGED BEHAVIOR

A. Time-averaged rheological behavior toward the jamming transition

First we focus on the time-averaged probe particle motion and flow behavior, where spatiotemporal fluctuations are averaged out by time averaging.

First we focus on the time-averaged rheological properties of a system. We investigate how the drag coefficient diverges when the volume fraction approaches the jamming point Φ_J under a fixed driving force of $F = 0.5$. We discuss the nonlinear behavior of athermal suspensions, i.e., the yielding behavior and the driving-force dependence of the time-averaged drag coefficient, in Sec. VI. Figure 1(a) shows the Φ dependence of the drag coefficient of the FPD simulations for different system sizes L. The drag coefficient C_D steeply increases with an increase in Φ and tends to diverge toward Φ_J. In the inset of Fig. 1(a), we can see a clear finite-size effect: The drag coefficient is larger for a smaller system size due to the stronger confinement of flow (see Appendix A). In Figs. 1(c) and 1(d), we calculate the time-averaged flow, $\langle \boldsymbol{v}(\boldsymbol{r}, t)/\bar{V}_p\rangle_t$, where $\bar{V}_p$ is the average velocity of the probe particle, and see that it has a dipolar vortex pattern [51], which is apparently the same as the one created around a driven isolated particle in the steady state. We can also see that its spatial pattern is independent of Φ [compare Fig. 1(c) for $\Phi = 0.30$ and Fig. 1(d) for $\Phi = 0.65$], and constrained by the system size L. It is worth stressing that the relevant length scales characterizing the macroscopic averaged flow field in our system are only the particle size a_p and the system size L. Thus C_D should be a function of their ratio L/a_p alone.

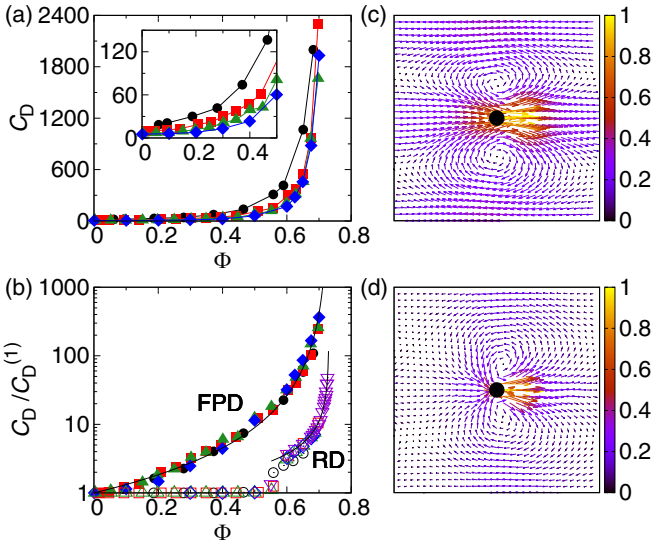

FIG. 1. Divergence of the time-averaged drag coefficient toward jamming. (a) The drag coefficient of the probe particle at $F = 0.5$ as a function of Φ in FPD for $L = 64$ (black circles), $L = 128$ (red squares), $L = 256$ (green up-triangles), $L = 512$ (blue diamonds). The inset shows the results in dilute regions. The solid lines are guides to the eyes. (b) The drag coefficients normalized by that in the dilute limit for FPD (solid symbols) and RD (open symbols) at $F = 0.5$. Purple down-triangles are the results for RD with $L = 1024$. The solid lines describe the fit by Eq. (16) (see text). [(c) and (d)] The time-averaged flow fields scaled by the average probe velocity $\bar{V}_p$ for FPD at $\Phi = 0.30, 0.65$, respectively. The probe particle is dragged in the direction of the right hand. Boxes are 256×256. We note that the time-averaged data are obtained by time averaging over a long time, during which the probe particle moves over at least several times of the system size.

For an isolated particle, it is known that the drag coefficient is affected by the finite-size effect as [64]

$$C_D^{(1)}(L) = \frac{4\pi\eta_s}{\log(L/a_p) - \lambda + \pi a_p^2/L^2}, \tag{15}$$

where $\lambda \simeq 1.3105$ (see Appendicies A and B and Fig. 8). The fact that the time-averaged flow pattern in dense suspensions is essentially the same as that for an isolated particle indicates that we may replace η_s by the effective viscosity $\eta_{\rm eff}(\Phi)$ in Eq. (15) even for a dense suspension of the volume fraction Φ by renormalizing the effects of disturbance of flow by host particles. As will be shown later, however, it is worth stressing here that although the time-averaged flow pattern has a symmetric dipolar vortex shape, the flow pattern in dense suspensions is strongly fluctuating spatiotemporally, or there is no steady state.

Based on the above argument, we can now remove the finite-size effect even at a high volume fraction Φ by scaling the drag coefficient of the probe particle $C_D(L)$ by the one without the other particles, i.e., a single-particle drag coefficient $C_D^{(1)}(L)$ for the system with the same size L. Indeed, we can see in Fig. 1(b) that, after the scaling, all the scaled time-averaged drag coefficients obtained in various system sizes fall onto a single master curve in the entire Φ range studied: $C_D(L)/C_D^{(1)}(L) \equiv C_D/C_D^{(1)}(\infty)$. This validity of the scaling strongly suggests a key physical nature of hydrodynamic interactions, i.e., the absence of screening effects and the presence of long-range cumulative correlation. Here we used the term "cumulative" to express the special hierarchical nature of hydrodynamic interactions.

In Fig. 1(b), we also plot the drag coefficient obtained by RD. The drag coefficients just below the jamming in the RD case are much less than those in the FPD case approximately by one order of magnitude. We will discuss the origin of this drastic difference later. Here we note that the RD data below $\Phi_c \cong 0.5$ has no physical meaning since, under the periodic boundary condition, the trace of the probe particle creates an empty path, or a tunnel, in which the probe particle passes through without any interaction with the other particles.

Figure 1(b) tells us that the scaled drag coefficient $C_D/C_D^{(1)}$ for both FPD and RD steeply diverges toward the jamming point Φ_J obeying the following power-law functions:

$$C_D(\Phi) = C_D^{(1)}[(\Phi_J - \Phi)/\Phi_J]^{-\alpha_X}, \tag{16}$$

where Φ_J and α_X (X = FPD or RD) are positive fitting parameters. Note that $\lim_{\Phi\to 0}(C_D(\Phi)/C_D^{(1)}) = 1$. Fitting to the data yields $\Phi_J = 0.73$, $\alpha_{\rm FPD} = 1.9$, and $\alpha_{\rm RD} = 0.76$. This critical volume fraction Φ_J is significantly less than the random close packing fraction of a 2D rigid sphere system, $\Phi_{\rm rcp} \simeq 0.84$ [65] due to the soft nature of the power-law potential, which we employed [see Eq. (1)]. We note that we use the common value for Φ_J for RD and FPD for simplicity, but there might be a small difference in the value reflecting the difference in the the main source of momentum dissipation.

Here we note that the value of the exponent $\alpha_{\rm FPD}$ is close to 2, which was reported by Boyer *et al.* [13] for macroscopic shearing of a granular suspension immersed in a viscous fluid. However, since the difference in the spatial dimensionality (3D vs. 2D), the type of perturbation (macroscopic vs. local) and the friction (with and without friction) between their and our cases may lead to a large difference in the particle collision behavior and macroscopic flow pattern between the two cases. Thus, the comparison is not straightforward and we leave the relation between the two exponents for future study.

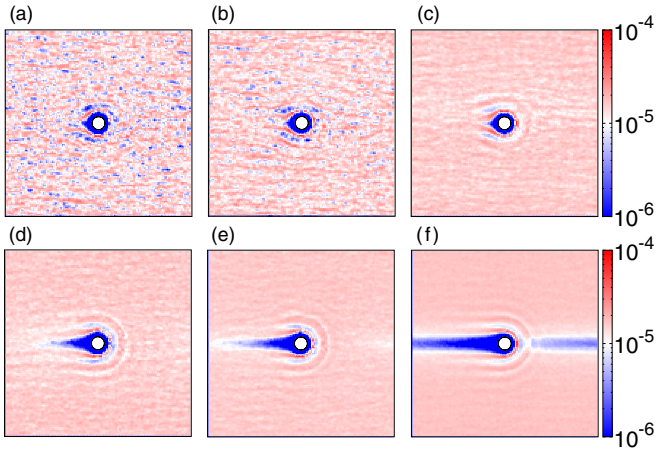

FIG. 2. Time-averaged density distribution around the probe particle at $F = 0.5$, 1.0, and 1.5 for the FPD [(a)–(c)] and RD [(c)–(e)] cases for $\Phi = 0.65$ and $L = 256$.

The difference in the divergence behavior of the drag coefficient toward Φ_J between FPD and RD can be qualitatively explained as follows (see below on more details): The viscous resistance steeply increases with an increase in Φ since fluid flow is more strongly confined between narrow channels among host particles. We stress that the degree of the enhancement of the drag coefficient $C_D(\Phi, L)$ depends only on Φ once it is scaled by $C_D^{(1)}(L)$, as shown in Fig. 1(b).

B. Density distribution around the probe particle in motion

Next we discuss the density distribution of host particles around the driven probe particle. Previous studies pointed out that thinning phenomena are accompanied by fore-aft asymmetry in the density distribution around the probe particle [44,47,48]. Here we consider whether this statement is really applied to dense granular suspensions. We compare the time-averaged density distribution around the moving probe particle in Fig. 2 for the FPD and RD cases with different values of F in a range of force thinning behavior [see Figs. 7(a) and 7(b)]. Here "force thinning" means that the decrease of the drag coefficient with an increase in the drag force [41,49], in the meaning similar to shear thinning. For the FPD case, there is little asymmetry in the density distribution around the probe particle for any drag forces employed [see Figs. 2(a)–2(c)]. For the RD case, on the other hand, there is significant fore-aft asymmetry and its magnitude grows monotonically as the drag force is increased [see Figs. 2(d)–2(f)]. This clearly indicates that the thinning behavior in the FPD case is not associated by the asymmetry in the density distribution. This preservation of the fore-aft symmetry is a consequence of the incompressibility of a fluid, which induces back flow [see Figs. 1(c) and 1(d)].

C. Force transmission

Next we focus on the average information on the force transmission and the motion of host particles. Since force chains directly affect the motion of the dragged particle via the momentum conservation, we characterize how the stress

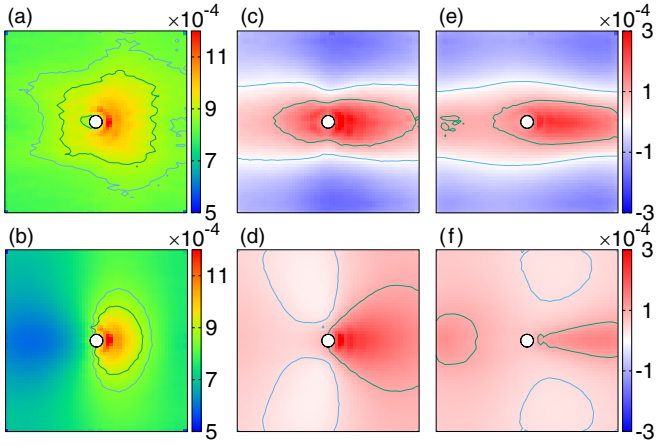

FIG. 3. Time-averaged pressure and host-particle motion around the probe particle for $\Phi = 0.65$, $L = 256$, and $F = 0.5$. Spatial correlation of particle pressure between the probe and the host particles for FPD (a) and RD (b). Spatial correlation of the particle displacement between the probe and host particles for FPD [(c) and (e)] and RD [(d) and (f)]. The average displacements of the probe particle are $\Delta l_p = 0.625a_p$ [(c) and (d)] and $\Delta l_p = 15.6a_p$ [(e) and (f)]. Boxes are all 256×256.

exerted by the probe particle transmits via force chains, by looking at the spatial correlation of local pressure. As a measure of the strength of interparticle force, we calculate the particle contribution on the stress tensor defined as

$$\sigma^i_{\alpha\beta}(t) = \frac{1}{2}\sum_j F^{ij}_\alpha(t) R^{ij}_\beta(t), \tag{17}$$

where R^{ij}_α is the α component of the interparticle vector between particle i and particle j and F^{ij}_α is the repulsive potential force between them. The trace of the stress tensor is proportional to the potential between the two particles, $U(\boldsymbol{R}_{ij})$, used in this study. The correlation between the pressure on the probe and that on host particles can be expressed by the following field:

$$G_p(\boldsymbol{r}) = \left\langle \sum_{i\neq 1} \frac{\sigma^p_{\alpha\alpha}(t)\sigma^i_{\alpha\alpha}(t)}{|\sigma^p_{\alpha\alpha}(t)|^2} \delta(\boldsymbol{r} - \boldsymbol{R}_i(t) + \boldsymbol{R}_p(t)) \right\rangle_t. \tag{18}$$

Here $\sigma^p_{\alpha\alpha}$ represents the $\alpha\alpha$ stress component of the probe particle. The repeating indices mean the summation.

We show the spatial correlation of local pressure in Figs. 3(a) and 3(b) for FPD and RD, respectively. Host particles involved in instantaneous force chains directly acting on the probe particle contribute to the strong correlation in the front part of the probe particle. We can see that the pressure transmission range is longer for FPD than for RD [see Figs. 3(a) and 3(b)]. This should arise from the difference in the stabilization mechanism of force chains between the two. For RD, a force chain is stabilized only by a proper geometrical arrangement of particles under a mechanical balance condition. For FPD, on the other hand, there is an additional stabilization mechanism: Force chains can be stabilized by fluid flow confined in narrow channels between particles because the incompressibility of the fluid tends to inhibit the local rearrangement of the host particles forming the force chains. This can be regarded as hydrodynamic organization (or stabilization) of force chains. We also note that the correlation behind the probe particle in FPD is much stronger than that in RD [see Figs. 3(a) and 3(b)]. This is because in FPD host particles are transported by the dipolar vortexlike flow as a consequence of the incompressibility of the fluid [see Fig. 1(d) at the same Φ], which leads to interparticle collisions and the resulting force chain formation even behind the probe particle [see also Figs. 4(f)–4(h)].

D. Average motion of host particles

The existence of a fluid also significantly affects the motion of host particles around the probe particle. By using the displacement vector defined as $\boldsymbol{u}_i(t;\Delta t) = \boldsymbol{R}_i(t+\Delta t) - \boldsymbol{R}_i(t)$, we calculate the spatial correlation between the displacement vector of the probe particle and those of host particles:

$$G_u(\boldsymbol{r};\Delta t) = \left\langle \sum_{i\neq 1} \frac{\boldsymbol{u}_p(t;\Delta t)\cdot\boldsymbol{u}_i(t;\Delta t)}{|\boldsymbol{u}_p(t;\Delta t)|^2} \delta(\boldsymbol{r} - \boldsymbol{R}_i(t) + \boldsymbol{R}_p(t)) \right\rangle_t. \tag{19}$$

Here $\boldsymbol{u}_p(t;\Delta t)$ represents the displacement vector of the probe particle.

Figures 3(c)–3(f) show such correlations for different iteration times Δt, by which we characterize the average displacement Δl_p of the probe particle during Δt as $\Delta l_p = \bar{V}_p \Delta t$. In FPD, even when the average displacement is quite small ($\Delta l_p = 0.625a_p$), there is a region where the correlation is negative (blue regions), indicating the presence of back flow of host particles [Fig. 3(c)]. Thus, the distribution of host particles is rather homogeneous: There is obvious asymmetry around the probe particle in the development of force chains and viscous dissipation rate but not in the spatial distribution of host particles, unlike RD (see Fig. 2). The increase in the average probe displacement does not alter the basic characteristics of the correlation, although it slightly increases the anisotropy [Fig. 3(e) with $\Delta l_p = 15.6a_p$].

In RD, on the other hand, the correlation at small Δl_p is very weak behind the probe particle [see Fig. 3(d) with $\Delta l_p = 0.625a_p$], reflecting that there is no mechanism for host particles behind to interact with the probe particle. For an iteration time during which the probe particle moves over a longer average distance ($\Delta l_p = 15.6a_p$), the highly correlated region is confined in a narrow direction along the drag direction for RD, as shown in Fig. 3(f). Since there is no backflow due to the absence of fluid flow, a depleted region, or a void, is formed behind the probe particle [see Fig. 2 and Figs. 4(i)–4(k)]. This difference in the density profile of host particles around the probe particle between FPD and RD (nearly isotropic vs. strongly anisotropic) is a direct consequence of the incompressibility of the fluid: For RD, there exist only short-range interactions through the interparticle potential, which allows only local rearrangement of host particles. In FPD, the global rearrangement of particle configuration, or the motion of most of host particles, is induced by the motion of the probe particle via nonlocal hydrodynamic interactions, which is responsible for the drastic enhancement of the drag coefficient [see Fig. 1(b)].

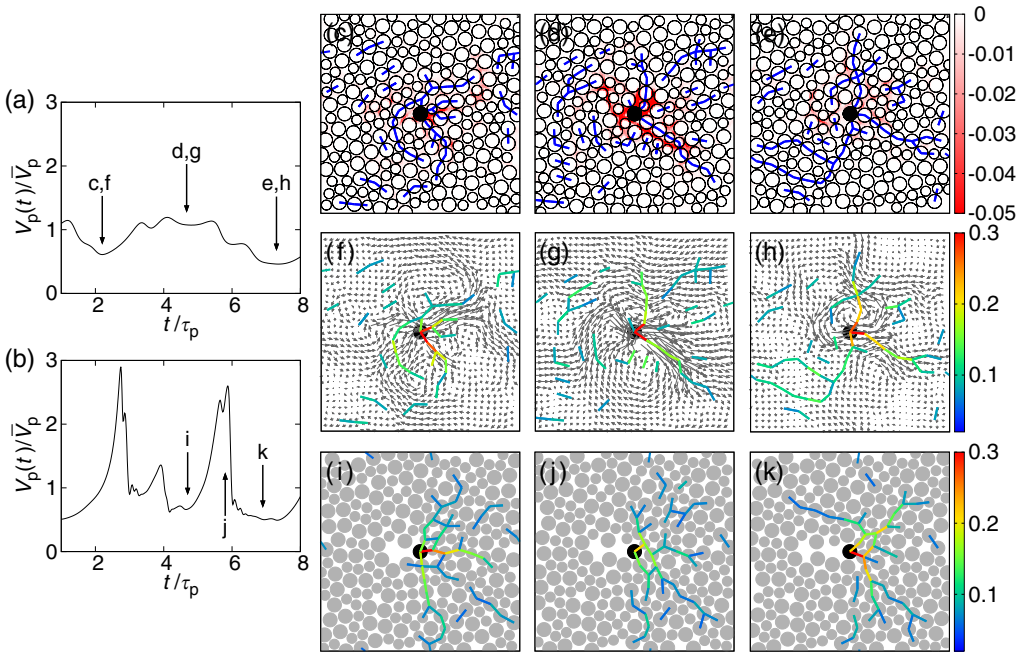

FIG. 4. Dynamic fluctuations of the velocity of the probe particle. Temporal fluctuations of the probe velocity with (a) and without hydrodynamic interactions (b) for $\Phi = 0.65$, $L = 256$, and $F = 0.5$. Here we scale the time t by the characteristic time of the probe motion, $\tau_p = a_p/\bar{V}_p$. We also show spatiotemporal fluctuations of the particle configurations and viscous dissipation in (c)–(e) and the fluid velocity field and force chains in (f)–(h) for the system with hydrodynamic interactions at the timings indicated in (a). In (f)–(h), interparticle forces are indicated by the line segments which are colored according to their strength (the more red, the stronger the force) and the velocity field of the fluid is depicted by arrows (the longer the arrow, the faster the velocity). In (i)–(k), we show the particle configuration and force chains (the meaning of the color is the same as in (f)–(h)) in the system without hydrodynamic interactions at the timings indicated in (b). Boxes are all 256×256.

V. IMPACT OF HYDRODYNAMICS ON THE PROBE PARTICLE MOTION IN DENSE SUSPENSIONS: SPATIOTEMPORAL FLUCTUATIONS

Now we focus on the spatiotemporal fluctuations of the probe particle motion and flow behavior.

A. Intermittency of the motion of the probe particle

1. Intermittency and its relation to force chains and flow

So far we focused on the time-averaged behavior of the probe particle motion, but actually the motion has strong spatiotempeoral fluctuations for both RD and FPD, which we can clearly see in Figs. 4 and 5. In Figs. 4(a) and 4(b), we compare dynamical fluctuations of the velocity of the probe particle along the drag direction between the two at $\Phi = 0.65$. We also show a series of snapshots of force chains in the corresponding courses of the motion together with flow fields in Figs. 4(c)–4(k).

In RD, the probe velocity is directly correlated to the structure of the force chains: when strong force chains are formed just in front of the probe particle, the probe velocity decreases as in Figs. 4(i) and 4(k); otherwise, the probe particle moves rapidly as in Fig. 4(j). The shape of the temporal change of the probe velocity is sawtoothlike, reflecting gradual development of force chains and their sudden collapse. This suggests that particles directly interacting with the probe particle in the form of force chains mainly contribute to the drag coefficient or the dissipation via the local friction constant [22]. The number of involved particles monotonically increases with an increase in the volume fraction and diverges when the force network is percolated at the jamming point [55]. Furthermore, the probe velocity fluctuations steeply increases with Φ, reflecting the temporal development of force chains [see Fig. 6(a)].

In contrast to RD, there is no such direct correlation between the probe velocity and the structure of force chains for FPD. The pattern of the temporal change of the probe velocity becomes rather continuous due to nonlocal hydrodynamic flow. Space-spanning dipolar vortices develop when the probe

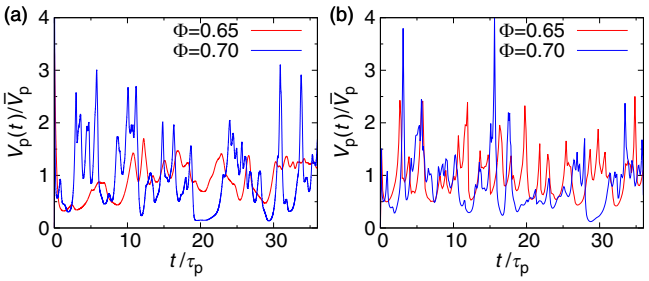

FIG. 5. Temporal fluctuation of the probe particle velocity. [(a) and (b)] Temporal change of the scaled probe velocity at $\Phi = 0.65, 0.7$ for the FPD and RD methods ($L = 256$ and $F = 0.5$), respectively. The velocity and the time is scaled by the average probe velocity $\bar{V}_p$ and the characteristic time over which the probe particle moves by its radius, $\tau_p = a_p/\bar{V}_p$, respectively.

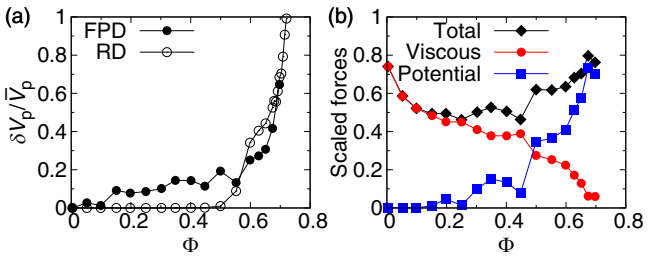

FIG. 6. Characteristics of the Φ dependence of the rheological response for $L = 256$ and $F = 0.5$. (a) Φ Dependence of the standard deviation of the probe velocity fluctuations $\delta V_p (= (\langle [\boldsymbol{V}_p(t) - \bar{\boldsymbol{V}}_p]^2 \rangle_t)^{1/2})$ scaled by $\bar{V}_p$ for FPD. (b) Decomposition of the force acting on the probe particle into the solid and fluid components for FPD. The components are scaled by the effective drag force $F_{\rm eff}$. We note that the time-averaged data are obtained by time averaging over a long time, during which the probe particle moves over at least several times of the system size.

velocity is increased as in Fig. 4(g) [compare it with Figs. 4(f) and 4(h)], but its pattern is strongly distorted compared to the time-averaged one at the same Φ [e.g., Fig. 1(d)]. Contrary to an expectation that the fluid flow may be largely suppressed in highly packed suspensions via screening effects, we find that the velocity field is always highly nonlocal and correlated over the system size, as shown in Figs. 4(f)–4(h). The fluid motion rather than the motion of host particles involved in the force chains is the main source of dissipation and thus the key contributor to the drag coefficient for $\Phi < 0.5$ [Fig. 6(b)]. However, for $\Phi \geqslant 0.5$, direct interparticle interactions start to become more dominant [Fig. 6(b)], and accordingly the amplitude of the probe velocity fluctuations steeply increases but its value scaled by the average probe velocity is less than in RD due to the nonlocal transportation [Fig. 6(a)].

2. The nature of the temporal fluctuations of the probe velocity

The above result indicates that the incompressibility of the interstitial fluid leads to the global rearrangement of host particles over a long distance for FPD. This qualitatively explains the stronger enhancement of the drag coefficient for FPD than RD [Fig. 1(b)], and the weaker temporal fluctuations of the probe particle motion [see Figs. 4(a) and 4(b)].

Here we consider the nature of the temporal fluctuation of the probe velocity, focusing the difference between the RD and FPD cases. In the RD case, the probe velocity is directly controlled by force chains, as shown above. Reflecting the formation and collapse of force chains in front of the probe particle, the pattern of the temporal change of the probe velocity is always sawtoothlike independent of Φ. In the FPD case, on the other hand, the inconsistency between the particle configuration of a stable force chain and the vortexlike fluid flow and the delocalized nature of flow weakens the intermittent nature of the probe motion seen in the RD case and makes the velocity fluctuation weaker and more continuous.

Next we consider how the change in the volume fraction Φ affects the characteristics of the probe velocity fluctuation. The temporal change of the probe velocity is shown for $\Phi = 0.65, 0.7$ in Figs. 5(a) and 5(b) for the FPD and RD, respectively. In the RD case, the probe velocity fluctuates around its average with a similar sawtoothlike pattern for both Φ's, whereas in the FPD case the fluctuation pattern dramatically changes from a rather continuous pattern to a sawtoothlike one as Φ increases from 0.65 to 0.7. This is consistent with the increase of the mechanical contribution relative to the hydrodynamic one with an increase in Φ [see Fig. 6(b)].

B. Φ Dependence of velocity fluctuations of the probe particle

We can see in Fig. 6(a) that the magnitude of the velocity fluctuations of the probe particle steeply increases for both FPD and RD particularly for $\Phi \geqslant 0.5$ [see also Figs. 4(a) and 4(b)]. The intermittency is basically a consequence of the formation of force chains due to local densification by the drag force and their destabilization induced by the motion of the probe particle. A force chain can be stable only for a special chainlike configuration and very fragile against random perturbations particularly for frictionless particles. As will be discussed below, hydrodynamic flow has a strong impact on the stability of force chains.

For FPD, we can see that with an increase in Φ there is a gradual crossover from "hydrodynamics-dominating regime," where particles mainly interact via long-range cumulative hydrodynamic interactions without serious effects of direct interparticle potential overlaps and the resulting force chains, to "plastic regime," where collisions of the probe and surrounding particles and the resulting formation of force chains particularly in front of the probe lead to avalanche-like intermittent behaviors. This can be directly revealed by looking at the components of the force acting on the probe particles from host particles and the fluid. To do so, the viscous and potential force acting on the probe particle are calculated by the first and second terms in Eq. (10), respectively. In Fig. 6(b), we plot their magnitudes in the direction parallel to the driving force together with that of the total force. The nonmonotonic dependence of the total force as a function of the volume fraction ϕ might apparently look strange. This may originate from the nonmonotonic angular fluctuations of the motion of the probe particle: At low Φ, the direction of the probe motion less fluctuates, whereas at intermediate Φ it highly fluctuates by randomization of flow due to the presence of host particles. At high Φ, the direction of the probe motion is again constrained in a narrow angular range along the drag direction due to the compaction by host particles (while the velocity fluctuation is significantly large). We can also see in Fig. 6(b) that the solid force overwhelms the fluid force for $\Phi \geqslant 0.5$. This increase in the solid contribution with increasing Φ leads to the steep growth of the magnitude of the velocity fluctuations, or the intermittency, of the probe particle, particularly above $\Phi \sim 0.5$ [Fig. 6(a)].

The above comparison between FPD and RD immediately tells us that the FPD drag coefficient, or the energy dissipation, starts to increase at much lower Φ than the RD one. By definition, the dissipation should come only from a viscous fluid for FPD, whereas from the local friction for RD. For the latter, the total dissipation is simply given by $\Sigma_i (1/2)\zeta_i \boldsymbol{V}_i^2$. Viscous dissipation in FPD is much larger than that associated with the local friction ζ_i in RD, which is estimated for an isolated particle, because fluid flow is not only confined in narrow

channels between particles but also strongly delocalized over the entire system in FPD.

C. Physical factor controlling intermittent behavior

Now the remaining question is what controls the intermittent behavior of the probe motion for FPD. In FPD, the instantaneous drag coefficient of the probe particle is determined not only by the particle pressure exerted by host particles, i.e., force chains, but also by the viscous dissipation in the fluid through many-body hydrodynamic interactions. In order to elucidate the dissipation rate, we define the field of local and temporal velocity gradients in the fluid region as

$$\dot{\Gamma}_{\alpha\beta}(\boldsymbol{r},t)=\frac{\partial}{\partial r_\beta}v_\alpha(\boldsymbol{r},t)+\frac{\partial}{\partial r_\alpha}v_\beta(\boldsymbol{r},t).$$

The subscripts α,β indicates either x or y. As can be seen from Eq. (5), this quantity characterizes the velocity gradient relevant for viscous dissipation in the solvent. Then we can estimate the local viscous dissipation rate field in the fluid region as

$$\dot{E}_{\rm diss}(\boldsymbol{r},t)=\sum_{\alpha,\beta}\frac{1}{2}\eta_s\dot{\Gamma}^2_{\alpha\beta}(\boldsymbol{r},t). \tag{20}$$

In Figs. 4(c)–4(e), we show the spatial distribution of the momentum dissipation rate, $-10^6\dot{E}_{\rm diss}$, for $\Phi=0.65$ and $L=256$ together with instantaneous force chains. We can see a drastic increase in dissipation by formation of regions of high shear rate along the force chains when the speed of the probe particle increases [see Fig. 4(d)]. This indicates nontrivial dynamical coupling between localization of flow and force chains: When force chains are formed in directions close to that of the drag force, the probe velocity and the dissipation decrease [see Figs. 4(f) and 4(h)], whereas on destabilization of such force chains the particle velocity increases accompanying the enhanced flow field and the stabilization of force chains along the flow (not in the direction of the drag force).

For RD, the intermittent behavior is a direct consequence of destabilization of force chains due to collision-induced geometrical perturbations on them, which leads to spikelike acceleration of the particle motion. For FPD, on the other hand, the intermittent motion is also caused by the inconsistency between particle chain configuration organized by the vortexlike flow and the translational transportation of force chains by the dragged particle. For example, the stable straight configuration of force chains is not consistent with the vortex flow pattern that is favored hydrodynamically [compare them in Figs. 4(f)–4(h)]. Such an inconsistency is a destabilization factor of force chains. This process takes place rather slowly because of the nonlocal nature of hydrodynamic flow, leading to a rather smooth change in the particle velocity unlike RD [see Figs. 4(a) and 4(b)].

VI. NONLINEAR RHEOLOGICAL BEHAVIOR: YIELDING AND FORCE THINNING

So far we have fixed a drag force F. Here we consider how the response depends on F. We stress that, since our system is athermal, its response to an external drive is intrinsically nonlinear and there is no Newtonian regime at any Φ. To study the nonlinearity of the response to an external drive, we performed simulations with FPD and RD in the force range of $0.01\leqslant F\leqslant 10$ for $\Phi=0.65$ and $L=256$.

The jamming point under the external drive depends on the magnitude of the drive. For $F=0.01$ and 0.05, the probe particle does not move in both methods, indicating that the system is kept jammed for these values of F. We note that since particles interact via soft-core power-law potentials, force chains are weakly percolated over the whole system even at the volume fraction of $\Phi=0.65$. If the drag force is weaker than the average strength of the interparticle forces, then the probe particle cannot move. In other words, the stress exerted by these drag forces are below the yield stress of the system. The system yields for $F\geqslant 0.1$. The drag coefficient decreases by more than one order of magnitude for both FPD and RD when the drag force F is increased from 0.1 to 10 [Fig. 7(a)].

The mechanism for the thinning behavior of RD can be explained as follows. Force chains formed to support the drag force are destabilized by the motion of the probe particle whenever they are tilted from the direction of the drag force, since it inevitably leads to collisions with other particles. Such disturbance becomes stronger with an increase in the drag force. This leads to the decrease in both the drag coefficient and the magnitude of velocity fluctuations of the probe particle, as shown in Figs. 7(a) and 7(b), respectively. In addition to this physical mechanism, we should note that there is also an artifact for RD. As the drag force is increased, the particle rearrangement in the back of the probe particle cannot catch up with a rapid motion of the probe particle, leading to the formation of the void region [see Figs. 2(d)–2(f) and Figs. 4(i)–4(k)]. The tail of the void region is more elongated with an increase in the drag force, and eventually it exceeds the simulation box, or appears in the front part of the probe particle due to the periodic boundary condition. This artifact due to the boundary condition leads to an unphysical reduction of the drag coefficient for $F>1$.

For FPD, the basic thinning mechanism is similar to that for RD in the sense that the motion of the probe particle destabilizes force chains, but the difference arises from the impact of hydrodynamic interactions on this process. The dipolar vortexlike flow is maintained even when the drag force is increased [Figs. 7(c)–7(e)]: The basic spatial pattern of the scaled time-averaged flow, $\bar{\boldsymbol{v}}(\boldsymbol{r})=\langle\boldsymbol{v}(\boldsymbol{r},t)/\bar{V}_p\rangle_t$, is independent of the magnitude of the drag force. However, the standard deviation from the time average of the flow field, $\delta\boldsymbol{v}(\boldsymbol{r})=(\langle[\boldsymbol{v}(\boldsymbol{r},t)/\bar{V}_p-\bar{\boldsymbol{v}}(\boldsymbol{r})]^2\rangle_t)^{1/2}$, are quite sensitive to the increase in the drag force: The flow field deviates more significantly in the front region of the probe particle for a weaker drag force, or its magnitude monotonically decreases as the drag force is increased [Figs. 7(f)–7(h)]. This can also be seen in the degree of the probe velocity fluctuations shown in Fig. 7(b): The amplitude of the scaled fluctuations and the frequency both decrease with an increase in the drag force. As discussed above, force chains formed in the front of the probe particle tend to interfere the vortexlike flow pattern favored by hydrodynamics [Figs. 4(f)–4(h)]. On noting this, we infer that the decrease of the magnitude of the deviation with an increase in the drag force is a consequence of the fact that force chains are more efficiently destroyed by the stronger vortexlike flows as the drag force is increased. This

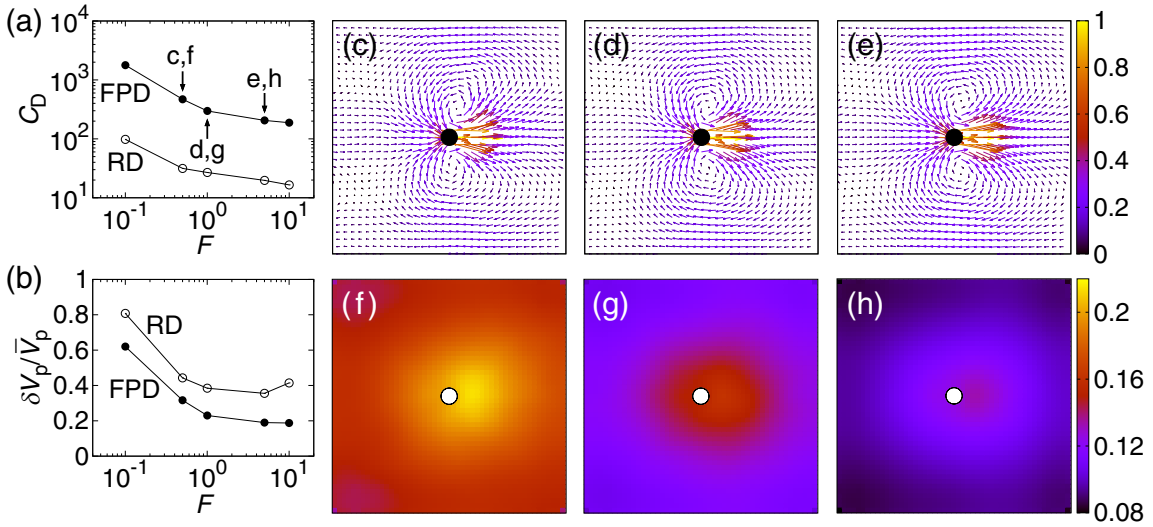

FIG. 7. Nonlinear rheological response. Drag coefficient (a) and the amplitude of probe velocity fluctuations (b) as a function of the magnitude of the drag force exerted on the probe particle for $\Phi = 0.65$ and $L = 256$. [(c)–(e)] The time-averaged velocity field in FPD for the three driving forces indicated in (a). [(f)–(h)] The field of the standard deviation from patterns shown in (c)–(e), respectively, with the same color bar. Boxes are all 256×256. We note that the time-averaged data are obtained by time-averaging over a long time, during which the probe particle moves over at least several times of the system size.

should also lead to the decrease of the velocity fluctuations or the intermittency of the probe particle motion, with an increase of F [Fig. 7(b)]. On the other hand, the decrease in the frequency of the fluctuations with an increase in the drag force, which is confirmed by a comparison of time evolution of the probe particle velocity for different drag forces and its Fourier transform, may be a consequence of the decrease of the stability of force chains. Less-stable force chains in the strong flow result in rather slow stress change relatively to the rapid probe particle motion. In this respect, this situation at a higher driving force is effectively similar to that at a lower volume fraction. Then the decrease of the drag coefficient, or viscous dissipation, with an increase in the drag force can be explained as follows: When the drag force is increased, the probe particle, or the center of the vortex flow, moves more rapidly. However, host particles forming force chains are left behind and deformed by the vortexlike flow in a direction perpendicular to the chains, leading to the collapse of the force chains. This collapse rate increases with the flow strength, leading to the decrease in the drag coefficient. We also note that, unlike in RD, density modulations (or, void formation) near the probe particle are minor due to long-ranged transportation of host particles by nonlocal flow. In other words, there is little apparent asymmetry induced by the directional motion of the probe particle even in the nonlinear thinning regime [see Figs. 2(a)–2(c)]. Thus, the large asymmetry in the particle density is not observed for dense suspensions, unlike the case of dry granular matter [66].

VII. CONCLUSION

In summary, we find that nontrivial spatiotemporal coupling between particles and a fluid plays an essential role in the rheological response of dense athermal suspensions to an external drive. Its importance can be seen most obviously from the fact that the way of the divergence of the drag coefficient of a probe particle toward the jamming point is largely different between with and without hydrodynamic interactions and its value can differ by more than one order of magnitude near the jamming point [see Fig. 1(b)]. Such dynamical coupling is a consequence of momentum conservation under the incompressible condition, which should be always satisfied at a low Reynolds number. We also reveal that reflecting the coexistence of solid and liquid components, momentum conservation has two distinct impacts of solid and fluid nature on the rheology. So far the rheology of dense suspensions have been discussed mainly from the mechanical aspect (i.e., force chains). However, our study strongly suggests the general importance of hydrodynamic degrees of freedom in nonlinear rheological behaviors of suspensions such as shear thinning and thickening. Its ignorance might lead to wrong conclusions even on a qualitative level. The nature of the coupling may also depend on the type of flow, shear or extensional flow.

In this paper, we study 2D systems to reduce the numerical cost. It is obviously interesting to study the effect of spatial dimensionality. We stress that both the hydrodynamic stabilization of force chains and the emergence of the dipolar voltex nature of the averaged flow are a direct consequence of the incompressibility of the fluid. In general, constraint on the fluid motion due to the incompressibility is weaker in 3D than in 2D because of the presence of an extra escape dimension for the former. This may make the difference in the drag coefficient between FPD and RD weaker for 3D than for 2D, but the enhancement of the drag coefficient by hydrodynamic interactions should exist even in 3D. Another interesting question is the role of thermal noise. The introduction of thermal noise should lead to the emergence of a linear regime for a sufficiently weak drag force, which is absent in the athermal system. This should also result in

the well-known link between the viscosity in the Newtonian region and the diffusion constant. We expect that the basic behavior at high volume fractions is dominated mechanically and thus the effect of thermal noise may be negligible. We leave the effects of the spatial dimensionality and the thermal noise for future investigation.

We hope our finding sheds new light on the complex nonlinear rheological behaviors of dense suspensions, which are crucial for many industrial applications and geological phenomena.

ACKNOWLEDGMENTS

This work was partially supported by Grant-in-Aid for Specially Promoted Research (25000002) and Scientific Research (A) (18H03675) from the Japan Society for the Promotion of Science (JSPS), and S.Y. was supported by Grant-in-Aid for JSPS Research Fellow (15J09476).

APPENDIX A: FINITE-SIZE EFFECT

The finite-size effect of the drag coefficient seen in the FPD simulation [see Fig. 1(a)] is of hydrodynamic origin. As we can see in Figs. 1(c) and 1(d), two vortices are formed symmetrically on both sides of the probe particle with opposite sign of vortices as a consequence of the conservation of the momentum. Because the size of the vortices is constrained by the system size L due to the long-range cumulative nature of hydrodynamic interactions, the curvature radius of the vortices is proportional to the system size L. This leads to the increase in the energy dissipation rate, resulting in the increase in the drag coefficient with a decrease in the system size L, as shown in Fig. 1(a). Furthermore, the structure of the flow pattern is maintained even for a supension of high particle density, as we can see in Figs. 1(c) and 1(d). Thus, the drag coefficient $C_D(L)$ can be scaled by that for a single dragged particle, $C_D^{(1)}(L)$, and the resulting scaled quantity $C_D(L)/C_D^{(1)}(L)$ is independent of the system sizes L for the entire range of the volume fraction Φ investigated, as shown in Fig. 1(b). This indicates that the incompressibility of the fluid plays a crucial role even in the highly concentrated region, where the system shows plastic behavior.

In the RD method, particles interact only due to the soft repulsive potential. In the plastic region, the behavior of host particles is controlled by force chains and direct interparticle collisions. The characteristic length of force chains is independent of the system size because of the short-range nature of the interactions as long as the percolation does not take place. The drag coefficient is, thus, approximated by the product of the friction coefficient and the number of host particles involved in force chains directly interacting with the probe particle. Therefore, the drag coefficient does not depend on the system size L [see Fig. 1(b)].

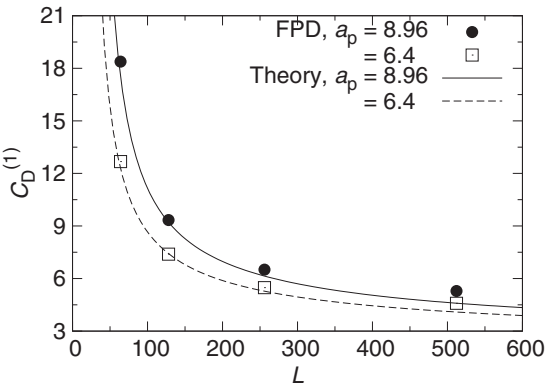

FIG. 8. Finite-size effect on a single-particle drag coefficient. The drag coefficient of a probe particle in a fluid (without host particles), $C_D^{(1)}$, are plotted as a function of the linear dimension L of the system for the two different sizes of the probe particle $a_p = 8.96$ and 6.4. Each point corresponds to the value shown in Table I. Solid and dashed lines represent the analytic functions by Eq. (15) for $a_p = 8.96$ and 6.4, respectively.

APPENDIX B: SINGLE-PARTICLE DRAG COEFFICIENT

We calculated a drag coefficient of a single isolated particle in a fluid (without host particles) by the FPD method, $C_D^{(1)}$, which is used for the constant friction coefficient in the RD simulations for each particle size and system size (see Sec. III). In a two-dimensional system, the drag coefficient differs from the Stokes friction, which is proportional to the particle size and fluid viscosity, and should have a logarithmic correction [67]. Furthermore, the drag coefficient suffer from the finite-size effect and is given by Eq. (15) [64]. The behavior of the drag coefficient calculated by the FPD method are shown in Fig. 8 as a function of the different system size and particle radius. The results agree well with the analytical relationships of Eq. (15), proving the numerical validity of the FPD method.

[1] H. M. Jaeger, S. R. Nagel, and R. P. Behringer, Granular solids, liquids, and gases, Rev. Mod. Phys. **68**, 1259 (1996).

[2] J. Mewis and N. J. Wagner, *Colloidal Suspension Rheology* (Cambridge University Press, Cambridge, 2012).

[3] P. Coussot, *Rheometry of Pastes, Suspensions, and Granular Materials: Applications in Industry and Environment* (John Wiley & Sons, New York, 2005).

[4] C. B. Holmes, M. E. Cates, M. Fuchs, and P. Sollich, Glass transitions and shear thickening suspension rheology, J. Rheol. **49**, 237 (2005).

[5] N. Huang, G. Ovarlez, F. Bertrand, S. Rodts, P. Coussot, and D. Bonn, Flow of Wet Granular Materials, Phys. Rev. Lett. **94**, 028301 (2005).

[6] L. Isa, R. Besseling, and W. C. K. Poon, Shear Zones and Wall Slip in the Capillary Flow of Concentrated Colloidal Suspensions, Phys. Rev. Lett. **98**, 198305 (2007).

[7] Y. Forterre and O. Pouliquen, Flows of dense granular media, Ann. Rev. Fluid Mech. **40**, 1 (2008).

[8] A. Lemaître, J. Roux, and F. Chevoir, What do dry granular flows tell us about dense non-brownian suspension rheology? Rheol. Acta **48**, 925 (2009).

[9] L. Isa, R. Besseling, A. N. Morozov, and W. C. K. Poon, Velocity Oscillations in Microfluidic Flows of Concentrated Colloidal Suspensions, Phys. Rev. Lett. **102**, 058302 (2009).

[10] N. J. Wagner and J. F. Brady, Shear thickening in colloidal dispersions, Phys. Today **62**, 27 (2009).

[11] A. Fall, F. Bertrand, G. Ovarlez, and D. Bonn, Yield Stress and Shear Banding in Granular Suspensions, Phys. Rev. Lett. **103**, 178301 (2009).

[12] A. Fall, A. Lemaitre, F. Bertrand, D. Bonn, and G. Ovarlez, Shear Thickening and Migration in Granular Suspensions, Phys. Rev. Lett. **105**, 268303 (2010).

[13] F. Boyer, É. Guazzelli, and O. Pouliquen, Unifying Suspension and Granular Rheology, Phys. Rev. Lett. **107**, 188301 (2011).

[14] S. Herminghaus, *Wet Granular Matter: A Truly Complex Fluid* (World Scientific, Singapore, 2013), Vol. 6.

[15] N. Y. C. Lin, B. M. Guy, M. Hermes, C. Ness, J. Sun, W. C. K. Poon, and I. Cohen, Hydrodynamic and Contact Contributions to Continuous Shear Thickening in Colloidal Suspensions, Phys. Rev. Lett. **115**, 228304 (2015).

[16] C. D. Cwalina and N. J. Wagner, Rheology of non-brownian particles suspended in concentrated colloidal dispersions at low particle reynolds number, J. Rheol. **60**, 47 (2016).

[17] D. Bonn, M. M. Denn, L. Berthier, T. Divoux, and S. Manneville, Yield stress materials in soft condensed matter, Rev. Mod. Phys. **89**, 035005 (2017).

[18] M. Ramaswamy, N. Y. C. Lin, B. D. Leahy, C. Ness, A. M. Fiore, J. W. Swan, and I. Cohen, How Confinement-Induced Structures Alter the Contribution of Hydrodynamic and Short-Ranged Repulsion Forces to the Viscosity of Colloidal Suspensions, Phys. Rev. X **7**, 041005 (2017).

[19] P. Coussot, *Mudflow Rheology and Dynamics* (Routledge, London, 2017).

[20] M. M. Denn, J. F. Morris, and D. Bonn, Shear thickening in concentrated suspensions of smooth spheres in newtonian suspending fluids, Soft Matter **14**, 170 (2018).

[21] C. Ness, R. Mari, and M. E. Cates, Shaken and stirred: Random organization reduces viscosity and dissipation in granular suspensions, Sci. Adv. **4**, eaar3296 (2018).

[22] M. E. Cates, J. P. Wittmer, J. P. Bouchaud, and Ph. Claudin, Jamming, Force Chains, and Fragile Matter, Phys. Rev. Lett. **81**, 1841 (1998).

[23] A. J. Liu and S. R. Nagel, Nonlinear dynamics: Jamming is not just cool any more, Nature **396**, 21 (1998).

[24] P. Coussot, Q. D. Nguyen, H. T. Huynh, and D. Bonn, Viscosity bifurcation in thixotropic, yielding fluids, J. Rheol. **46**, 573 (2002).

[25] P. C. F. Møller, J. Mewis, and D. Bonn, Yield stress and thixotropy: On the difficulty of measuring yield stresses in practice, Soft Matter **2**, 274 (2006).

[26] R. Seto, R. Mari, J. F. Morris, and M. M. Denn, Discontinuous Shear Thickening of Frictional Hard-Sphere Suspensions, Phys. Rev. Lett. **111**, 218301 (2013).

[27] R. Mari, R. Seto, J. F. Morris, and M. M. Denn, Shear thickening, frictionless and frictional rheologies in non-brownian suspensions, J. Rheol. **58**, 1693 (2014).

[28] M. Wyart and M. E. Cates, Discontinuous Shear Thickening Without Inertia in Dense Non-Brownian Suspensions, Phys. Rev. Lett. **112**, 098302 (2014).

[29] E. Brown and H. M. Jaeger, Shear thickening in concentrated suspensions: Phenomenology, mechanisms and relations to jamming, Rep. Prog. Phys. **77**, 046602 (2014).

[30] M. Hermes, B. M. Guy, W. C. K. Poon, G. Poy, M. E Cates, and M. Wyart, Unsteady flow and particle migration in dense, non-brownian suspensions, J. Rheol. **60**, 905 (2016).

[31] D. L. Koch and E. S. G. Shaqfeh, Screening in sedimenting suspensions, J. Fluid Mech. **224**, 275 (1991).

[32] E. E. Ballard and A. L. Kholodenko, Topological character of hydrodynamic screening in suspensions of hard spheres: An example of universal phenomenon, Physica A **388**, 3024 (2009).

[33] M. Doi and S. F. Edwards, *The Theory of Polymer Dynamics* (Oxford University Press, Oxford, 1988), Vol. 73.

[34] C. W. J. Beenakker and P. Mazur, Diffusion of spheres in a concentrated suspension: Resummation of many-body hydrodynamic interactions, Phys. Lett. A **98**, 22 (1983).

[35] C. W. J. Beenakker and P. Mazur, Diffusion of spheres in a concentrated suspension ii, Physica A **126**, 349 (1984).

[36] H. Tanaka and T. Araki, Simulation Method of Colloidal Suspensions with Hydrodynamic Interactions: Fluid Particle Dynamics, Phys. Rev. Lett. **85**, 1338 (2000).

[37] H. Tanaka and T. Araki, Viscoelastic phase separation in soft matter: Numerical-simulation study on its physical mechanism, Chem. Eng. Sci. **61**, 2108 (2006).

[38] A. Furukawa and H. Tanaka, Key Role of Hydrodynamic Interactions in Colloidal Gelation, Phys. Rev. Lett. **104**, 245702 (2010).

[39] A. Furukawa, M. Tateno, and H. Tanaka, Physical foundation of the fluid particle dynamics method for colloid dynamics simulation, Soft Matter **14**, 3738 (2018).

[40] S. Kim and S. J. Karrila, *Microhydrodynamics: Principles and Selected Applications* (Dover, New York, 2005).

[41] L. G. Wilson, A. W. Harrison, A. B. Schofield, J. Arlt, and W. C. K. Poon, Passive and active microrheology of hard-sphere colloids, J. Phys. Chem. B **113**, 3806 (2009).

[42] L. G. Wilson, A. W. Harrison, W. C. K. Poon, and A. M. Puertas, Microrheology and the fluctuation theorem in dense colloids, Europhys. Lett. **93**, 58007 (2011).

[43] L. G. Wilson and W. C. K. Poon, Small-world rheology: An introduction to probe-based active microrheology, Phys. Chem. Chem. Phys. **13**, 10617 (2011).

[44] T. M. Squires and J. F. Brady, A simple paradigm for active and nonlinear microrheology, Phys. Fluids **17**, 073101 (2005).

[45] A. S. Khair and J. F. Brady, Single particle motion in colloidal dispersions: A simple model for active and nonlinear microrheology, J. Fluid Mech. **557**, 73 (2006).

[46] J. W. Swan and R. N. Zia, Active microrheology: Fixed-velocity versus fixed-force, Phys. Fluids **25**, 083303 (2013).

[47] A. Meyer, A. Marshall, B. G. Bush, and E. M. Furst, Laser tweezer microrheology of a colloidal suspension, J. Rheol. **50**, 77 (2006).

[48] I. Sriram, A. Meyer, and E. M. Furst, Active microrheology of a colloidal suspension in the direct collision limit, Phys. Fluids **22**, 062003 (2010).

[49] T. Wang and M. Sperl, Thinning and thickening in active microrheology, Phys. Rev. E **93**, 022606 (2016).

[50] R. Weeber and J. Harting, Hydrodynamic interactions in active colloidal crystal microrheology, Phys. Rev. E **86**, 057302 (2012).

[51] J. Pesic, J. Z. Terdik, X. Xu, Y. Tian, A. Lopez, S. A. Rice, A. R. Dinner, and N. F. Scherer, Structural responses of quasi-two-dimensional colloidal fluids to excitations elicited by nonequilibrium perturbations, Phys. Rev. E **86**, 031403 (2012).

[52] Th. Voigtmann and M. Fuchs, Force-driven micro-rheology, Eur. Phys. J. Spec. Top. **222**, 2819 (2013).

[53] E. Nazockdast and J. F. Morris, Active microrheology of colloidal suspensions: Simulation and microstructural theory, J. Rheol. **60**, 733 (2016).

[54] E. Lorenz, V. Sivadasan, D. Bonn, and A. G. Hoekstra, Combined lattice–Boltzmann and rigid-body method for simulations of shear-thickening dense suspensions of hard particles, Comput. Fluids **172**, 474 (2018).

[55] J. A. Drocco, M. B. Hastings, C. J. Olson Reichhardt, and C. Reichhardt, Multiscaling at Point *J*: Jamming is a Critical Phenomenon, Phys. Rev. Lett. **95**, 088001 (2005).

[56] R. Albert, M. A. Pfeifer, A.-L. Barabási, and P. Schiffer, Slow Drag in a Granular Medium, Phys. Rev. Lett. **82**, 205 (1999).

[57] J. Geng and R. P. Behringer, Slow drag in two-dimensional granular media, Phys. Rev. E **71**, 011302 (2005).

[58] K. A. Reddy, Y. Forterre, and O. Pouliquen, Evidence of Mechanically Activated Processes in Slow Granular Flows, Phys. Rev. Lett. **106**, 108301 (2011).

[59] J. E. Hilton and A. Tordesillas, Drag force on a spherical intruder in a granular bed at low Froude number, Phys. Rev. E **88**, 062203 (2013).

[60] M. Pica Ciamarra, A. H. Lara, A. T. Lee, D. I. Goldman, I. Vishik, and H. L. Swinney, Dynamics of Drag and Force Distributions for Projectile Impact in a Granular Medium, Phys. Rev. Lett. **92**, 194301 (2004).

[61] M. B. Stone, R. Barry, D. P. Bernstein, M. D. Pelc, Y. K. Tsui, and P. Schiffer, Local jamming via penetration of a granular medium, Phys. Rev. E **70**, 041301 (2004).

[62] H. Katsuragi and D. J. Durian, Unified force law for granular impact cratering, Nat. Phys. **3**, 420 (2007).

[63] T. G. Mason and D. A. Weitz, Optical Measurements of Frequency-Dependent Linear Viscoelastic Moduli of Complex Fluids, Phys. Rev. Lett. **74**, 1250 (1995).

[64] H. Hasimoto, On the periodic fundamental solutions of the stokes equations and their application to viscous flow past a cubic array of spheres, J. Fluid Mech. **5**, 317 (1959).

[65] Y. Takehara and K. Okumura, High-Velocity Drag Friction in Granular Media Near the Jamming Point, Phys. Rev. Lett. **112**, 148001 (2014).

[66] I. C. Carpen and J. F. Brady, Microrheology of colloidal dispersions by brownian dynamics simulations, J. Rheol. **49**, 1483 (2005).

[67] H. Lamb, On the uniform motion of a spherein a viscous fluid, Phil. Mag. **21**, 112 (1911).